Journal of Materials Chemistry B

PAPER

View Article Online
View Journal

Cite this: DOI: 10.1039/c5tb01740h

Single-step electrospun TiO_2–Au hybrid electrodes for high selectivity photoelectrocatalytic glutathione bioanalysis†

Anitha Devadoss,‡[a] Asako Kuragano,[ab] Chiaki Terashima,*[ac] P. Sudhagar,‡[a] Kazuya Nakata,[abc] Takeshi Kondo,[abc] Makoto Yuasa[abc] and Akira Fujishima[ac]

Received 24th August 2015,
Accepted 12th November 2015

DOI: 10.1039/c5tb01740h

www.rsc.org/MaterialsB

Understanding the fundamentals of photoelectrocatalytic (PEC) biomolecular oxidation benefits the development of next-generation PEC biosensors. In this work, single-step electrospun titanium-di-oxide–gold (TiO_2–Au) hybrid nanofibers (HNF) are reported as being a potential candidate for PEC glutathione (GSH) bioanalysis. The chemical environment of TiO_2 and TiO_2–Au HNFs were studied with X-ray photoelectron spectroscopy and found to have a strong electronic interaction between TiO_2 and the Au nanoparticles (NPs). The PEC measurements revealed that the intramolecular backbone hydrogen bonding of GSH molecules predominantly contributes highly active Au–GSH bio-nano interfaces, which facilitate the PEC oxidation rate of GSH and thus enhance the photocurrent. Furthermore, the Au NPs present act as auxiliary electron transport channels resulting in enhanced charge collection at the external circuit. As a result, the TiO_2–Au electrode generated a two-fold higher photocurrent density of ~84.4 μA cm^{-2} in the presence of 0.5 mM GSH, where the pristine TiO_2 NFs displayed only a negligible influence. Likewise, the TiO_2–Au HNF electrode showed a higher sensitivity of 0.002 mM and a wide linear detection range between 0.022 mM and 0.7 mM, with a superior selectivity towards GSH bioanalysis over ascorbic acid and glucose at −0.33 V (*versus* silver/silver chloride) than that obtained with pristine TiO_2. The implications of these findings towards the development of a next-generation PEC biosensor are discussed.

Introduction

Semiconductor photocatalysis integrates a photoexcitation process and surface catalysis. The photoexcitation involves light absorption and charge carrier generation (e^- and h^+), while the surface catalysis concerns the utilization of a photogenerated carrier. Photocatalysis-based semiconductor technology has attracted considerable research interest for the purpose of effectively utilizing the solar energy in solar cells, solar fuel cells, and organic pollutant removal, and so on.[1–4] On a different level, the photoelectrochemical (PEC) process has become a new and promising analytical tool for the detection of biomolecules.[5–8] Fujishima and Honda explored the use of the light driven photosensitized water oxidation phenomenon[1] as a key tool for accessing photoholes at the valence band of a semiconductor for advanced oxidation of chemical components in the gas or liquid phase. In this context, PEC oxidation of biomolecules by the photogenerated holes at the valence band of the semiconductor is an interesting approach for PEC bioanalysis.[9] In the PEC biosensor, a charge transfer reaction (charge separation and recombination) between the photoactive material and analyte under light irradiation plays a vital role in defining the sensitivity and selectivity. It is widely recognized that titanium dioxide (TiO_2) exhibits remarkable photoelectrocatalytic activity and chemical stability in a neutral pH, which is the primary prerequisite for bioanalysis.[10,11] Furthermore, the key benefit of the high positive valence band position of TiO_2 [~3 V *versus* a normal hydrogen electrode (NHE)] compared to a water oxidation potential of ~1.2 V *versus* NHE might extend the application of PEC bioanalysis to a wide range of biomolecules.[12]

Over the past decade, TiO_2-based bioanalysis has demonstrated successful detection of various biomolecules. Recently, use of glutathione (GSH) bioanalysis is gaining momentum because GSH serves as a potential antioxidant against free radicals and thus plays a central role in detoxification and biotransformation of chemotherapeutic drugs.[13] More specifically, in conjunction with the detoxification enzymes such as glutathione peroxidase

[a] *Photocatalysis International Research Center, Research Institute for Science & Technology, Tokyo University of Science, 2641 Yamazaki, Noda, Chiba 278-8510, Japan. E-mail: terashima@rs.tus.ac.jp*
[b] *Faculty of Science and Technology, Tokyo University of Science, 2641 Yamazaki, Noda, Chiba 278-8510, Japan*
[c] *ACT-C/JST, 4-1-8 Honcho, Kawaguchi, Saitama, 333-0012, Japan*

† Electronic supplementary information (ESI) available: XRD, XPS and JV Plots. See DOI: 10.1039/c5tb01740h

‡ These authors contributed equally.

(GSH-Px), glutathione reductase, glutathione *S*-transferases and so on, GSH can be used to detoxify the effect of external toxic materials.[14,15] In this context, cancer cells are known to have a higher concentration of GSH, which hinders the efficiency of anticancer therapy by detoxifying the carcinogens and by consuming toxic free radicals generated by the therapy. Furthermore, the physiological concentrations of GSH are an excellent indicator of various disease risks in human. As elevated levels of GSH are closely associated with a number of diseases in humans including aging and cancer,[16–21] a number of methods, including electrochemical,[22,23] fluorescence[24] and luminescence,[15] have been developed to determine the levels of GSH in blood. Conventional methods of monitoring the GSH expression such as fluorescence and electrochemical detection techniques suffer from photo-bleaching and high over potential, respectively.[25,26] Thus, developing new technologies which are applicable for early and accurate detection of GSH expression at a much lower potential is, therefore, of utmost importance in clinical diagnosis, treatment and prognosis of tumors.

In the past decade, a lot of research has been devoted to exploiting TiO_2 photoelectrodes for PEC bioanalysis.[27–29] With the aim of promoting the visible light accessing capability, TiO_2 is integrated with visible light band gap materials [cadmium selenide (CdSe), cadmium telluride (CdTe) and carbon quantum dots (QDs)],[30,31] and/or doped with non-metals (nitrogen).[32] In this context, the first report on PEC based GSH bioanalysis using a porphyrin sensitized TiO_2 nanoparticle (NP) electrode was reported by Tu *et al.*[33] Besides improving the weak visible light reception at the electrodes modified with TiO_2 NPs, porphyrin sensitization also promoted photo-excited charge carrier generation and thus reduced the onset potential of PEC GSH oxidation to $\sim$0.2 V. Later, Tang *et al.* demonstrated PEC GSH oxidation using vertically grown one-dimensional TiO_2 nanowires (NWs).[34] These one-dimensional (1-D) TiO_2 nanowires were sensitized with "hemin" and coated with a co-catalyst (iridium(IV) oxide (IrO_2) NPs). Here, the hemin promoted the selectivity of GSH targets, and the IrO_2 NPs effectively enhanced the charge transfer kinetics. As a result, the modified TiO_2 NW showed a $\sim$100% increase of photocurrent compared to the pristine TiO_2 NWs. Compared to the single-phase TiO_2 photocatalysis, titanium dioxide–gold (TiO_2–Au) heterostructures have shown a higher photocurrent and increased charge separation.[35,36] Here, the infusion of metal NPs promotes the PEC activity of TiO_2 because the unique band bending resulting from the formation of a semiconductor–metal interface (Schottky junction) favors the separation of charge carriers. In general, the enhancement in the photocurrent generation is attributed to the presence of Au NPs which act as an "electron-sink" and thus reduce the charge recombination at the TiO_2. The direct assembly of Au NPs which promoted the photocatalytic performance of TiO_2 NWs because of the combined light scattering and reduced recombination has recently been reported.[4] Additionally, it is also reported that the surface plasmon resonance (SPR) of Au NPs, originating from the collective oscillation of surface electrons upon visible light irradiation, enhances the photocatalytic activity of the host metal oxide.[37–40] Recently, pre-synthesized powder-type platinum (Pt) decorated TiO_2 nanowhiskers were also demonstrated as being successful for GSH sensing.[41] Despite the reported biosensing performances, there is still great scope for sensitivity and selectivity improvement in PEC GSH bioanalysis which involves probing the nano–bio interfaces.

It is already known that the method of TiO_2–Au hybrid formation plays a significant role in controlling the activity of Au NPs. Priebe *et al.*[42] showed that the method of Au deposition controls the TiO_2–Au electronic interface and thus influences the photocatalytic reaction activity of TiO_2. Furthermore, overloading of Au NPs exhibits a detrimental light blocking effect at the TiO_2 surface.[43] Therefore, it is necessary to clearly understand the nano–bio interface to fully exploit the PEC activity of the TiO_2–Au hybrid nanomaterials for bioanalysis. With the ultimate goal of understanding the interactions at the nano–bio interfaces, single step, ready-to-use TiO_2–Au hybrid nanofiber (HNF) electrodes have been developed using an electrospinning technique for GSH bioanalysis. To the best of our knowledge, this is the first report on the PEC application of an electrospun TiO_2–Au hybrid electrode for PEC GSH detection. In this research, the feasibility of a single-step fabrication of multiple complex materials or nanocomposites[44,45] using electrospinning is exploited. Furthermore, the main advantage of using a highly interconnected 1-D nanofibrous framework (rapid electron transport pathways and their wide pore channels) is anticipated to enhance the bioanalyte percolation that might result in effective electrode/electrolyte nano–bio interfaces.[46] The PEC measurements revealed the superior performance of TiO_2–Au HNFs over the pristine TiO_2. Although the existence of Au NPs is generally recognized to improve the PEC activity of TiO_2, this work is anticipated to provide new insights into the biomolecular selectivity perfections at the nano–bio interfaces, which will unlock a new dimension in PEC bioanalysis.

Results and discussion

The mechanism of PEC GSH bioanalysis at TiO_2–Au HNF electrodes is illustrated in Scheme 1. The typical photoelectrocatalytic biomolecular oxidation process at the photoanode (TiO_2–Au HNFs) is explained as follows: upon solar light illumination, photogenerated charge carriers (e^- and h^+) are produced at the TiO_2–Au HNFs. The photoelectrons are transported to charge collector (fluorinated tin oxide: FTO) through TiO_2 nanofibre (NF) channels, whereas the photoholes are subsequently scavenged to the electrolyte interface, where the dispersed GSH molecules get oxidized.

Besides improving the visible light activity of TiO_2, the presence of Au NPs is anticipated to promote the adsorption of GSH molecules onto TiO_2–Au, which could improve the GSH oxidation and thus contribute additional oxidative electrons to the circuit. During this process, GSH is oxidized into glutathione disulfide (GSSG). As the increase in the photocurrent solely depends on the GSH oxidation, the concentration of GSH can be precisely quantified from the photocurrent enhancements.

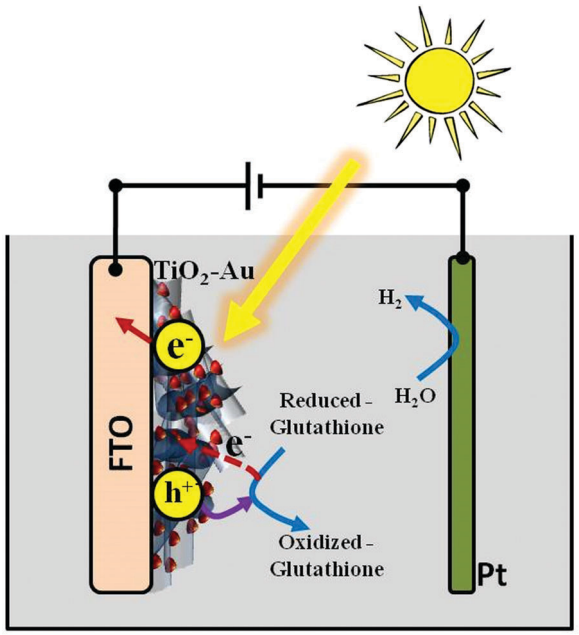

Scheme 1 Schematic illustration of photoelectrochemical cells for GSH sensing using a TiO_2–Au composite as photoanode and Pt wire as the counter electrode.

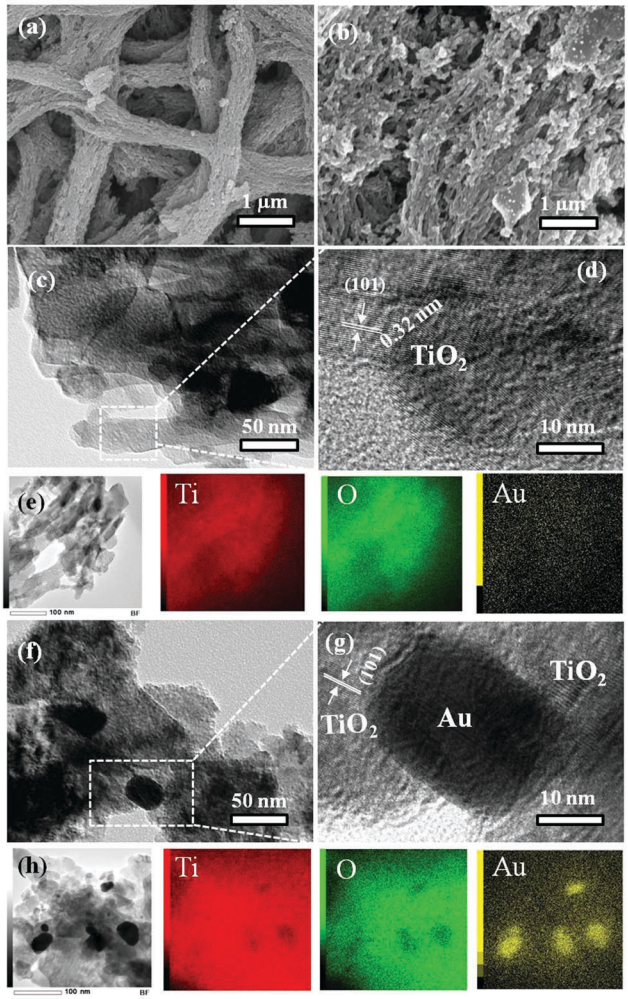

Fig. 1 Scanning electron microscopy images of (a) TiO_2 and (b) TiO_2–Au electrodes; transmission electron microscopy (TEM) image of TiO_2 (c) at 50 nm scale and (d) high magnification at 10 nm scale; (e) elemental mapping of Ti, O, and Au at a TiO_2 sample measured from Fig. 2(c); high resolution TEM image of TiO_2–Au (f) at 50 nm scale and (g) high magnification at 10 nm scale; (h) elemental mapping of Ti, O, and Au at TiO_2–Au composite at TiO_2–Au sample (f).

The crystallite structure of electrospun TiO_2 and TiO_2–Au HNFs on conducting substrates was examined using X-ray diffraction spectroscopy (XRD) and the results are presented in Fig. S1 [see ESI†]. From Fig. S1 (ESI†), the predominant peak observed at 25.3° in both samples confirm the (101) anatase crystallite phase. The remaining peaks seen at 37.6°, 47.6°, 53.8° and 54.8° correspond to (004), (200), (105) and (211) crystallite phases of TiO_2, respectively, (standard JCPDS of anatase TiO_2 (21-1272)). The significant crystallite peaks related to Au do not exist in the TiO_2–Au HNF electrode, which implies that Au NPs are impregnated at a very low concentration in TiO_2. The existence of the Au NPs is further investigated by comparing the peak width [full width at half maximum (FWHM)] values. It is inferred that the FWHM of TiO_2–Au crystallite peaks (101), (004) and (200) are narrower than those of pristine TiO_2, which confirms the presence of Au NPs at the TiO_2 lattice. The surface morphology and the elemental analysis of TiO_2 NFs and TiO_2–Au HNFs were examined using SEM (Fig. 1). The pristine TiO_2 electrode (Fig. 1a) shows the presence of highly interconnected 1-D TiO_2 fiber bundles with a mean diameter of 500–700 nm. These TiO_2 NF bundles are found to be formed by connecting the individual TiO_2 NPs. This can be attributed to the removal of polyvinylpyrrolidone (PVP) species from the as-synthesized TiO_2 NFs upon sintering at 500 °C, forming the porous sites that lead to the separation of individual spherical particles in the NF bundles.[47] Despite the similar fabrication conditions, the TiO_2–Au electrode (Fig. 1b) shows the formation of thinner NFs compared to pristine TiO_2. This may be ascribed to the simultaneous crystallization of Au NPs and TiO_2 during the sintering treatment and perhaps the PVP polymer species removal could facilitate the Au NPs diffusivity towards the porous sites at the TiO_2 bundles. This process might transform the thick TiO_2 bundle into thinner bundles. To further analyze the distribution of Au NPs in TiO_2 NFs, high magnification TEM images were recorded (Fig. 1c, d, f and g). The high magnification TEM image of the TiO_2 electrode (Fig. 1c) confirms that the interconnected structure of TiO_2 NFs is assembled from individual TiO_2 NPs (see ESI,† Fig. S2). From Fig. 1d, the estimated lattice diameter of ~0.32 nm confirms the presence of the anatase TiO_2(101) crystallite phase, which is in agreement with the XRD results (Fig. S1, ESI†). Additionally, Fig. 1f shows that Au NPs of ~15 nm in diameter are randomly incorporated in the TiO_2 crystallite and Fig. 1g clearly shows that the Au NP is bridging the TiO_2 crystals, which may be anticipated to enhance the charge transport along the TiO_2 channel. Elemental mapping of TiO_2 (Fig. 1e) and TiO_2–Au (Fig. 1h) samples confirm the presence of individual elements (Ti and O). A close proximity comparison between Fig. 1h and e strongly corroborates the presence of

Au NPs only in TiO_2–Au sample. As discussed earlier, the one-step precursor (metal and metal oxide) derived TiO_2–Au composite NFs show effective incorporation of Au NPs between the TiO_2 crystallite. The similar TEM observation on Au NPs incorporated TiO_2 crystallite is observed using a one-step hydrothermal technique.[48] Therefore, one-step electrospinning coating of TiO_2–Au directly onto the substrates results in effective dispersion of Au NPs in between the TiO_2 crystallite instead of decorating it on the surface.[49]

The chemical environment of TiO_2 NFs before and after Au NPs incorporation was studied using X-ray photoelectron spectrometry (XPS), and the results are presented in Fig. 2. From Fig. 2a, sharp shoulders observed at 458.8 and 464.6 eV correspond to the $Ti2p_{3/2}$ and $Ti2p_{5/2}$ orbitals and are further shifted ~0.4 eV towards the lower binding energy region upon Au NP incorporation. The atomic ratio of Ti, O and Au elements were estimated from the XPS results (see ESI,† Table T1). The asymmetric nature of the O1s peak is separated into symmetric multiple peaks using Gaussian transformation fitting after background correction (see ESI,† Fig. S3). The quantity of Ti is reduced from 57.3% to 50.6% after Au incorporation, which implies the diffusivity of Au NPs at the TiO_2 fiber and that they occupy space in between TiO_2 as is observed from the TEM image (Fig. 1g). Wang *et al.* reported a similar Ti2p peak shift in Ag NP incorporated TiO_2.[50] The O1s core spectra of pristine and Au incorporated TiO_2 are presented in Fig. 2b. In TiO_2, three significant peaks (ESI,† Fig. S3a) were identified at 529.7, 530.6, and 531.6 eV, where the first two peaks are assigned to lattice oxygen bound to Ti^{4+} and the third peak is attributed to the hydroxyl groups of TiO_2. After Au NPs incorporation, a small peak was noticed at 532.2 eV implying the possibility of water molecules adsorbed on TiO_2.[51] This enhanced hydrophilic property of TiO_2–Au HNFs is anticipated to result in high photocatalytic activity. The presence of Au at TiO_2 and their bonding nature with TiO_2 is further examined using Au4f core spectra (Fig. 2c). The strong shoulders appearing at 83.3 and 87.0 eV are assigned to $Au4f_{7/2}$ and $Au4f_{5/2}$, respectively.[52,53]

The quantity of Au was estimated from Fig. 2c and was found to be 7.59% and the atomic ratio of Au/Ti was 0.15. The first peak, $Au4f_{7/2}$ at 83.3 eV represents Au^0 bound at an oxygen vacancy (O^-) in the form of Au–$V^{\bullet\bullet}$.[54] It is known that oxygen vacancies formed in TiO_2 during sintering treatment act as Au nucleation sites.[55] The electrons initially belonging to the O_2^- ions contribute partially to the bond formation between Au and the defect site. Thus, the binding energy of this Au–$V^{\bullet\bullet}$ state is decreased by a negative charge transfer from the defective TiO_2 surface to the Au. Therefore, the binding energy between TiO_2 and Au through oxygen vacancies plays a crucial role in the catalysis reaction and charge transfer. The optical absorption spectra [Kulbelka–Munk (K.M.)] of both TiO_2 and TiO_2–Au HNFs are shown in Fig. 3. The K.M. absorption of TiO_2 shows the strong absorption peak around 375 nm, which is attributed to the absorption of titania. After the inclusion of Au NPs in TiO_2, a strong absorption shoulder around 550 nm was observed, corresponding to the SPR band of the Au NPs. The broad absorption peak indicates that the *in situ* formation of Au NPs in the TiO_2 nanofibrous network resulted in the formation of randomly size distributed Au NPs.

To investigate the photoelectrocatalytic property of pristine TiO_2 and TiO_2–Au HNFs, the current density–voltage (*J–V*) plots

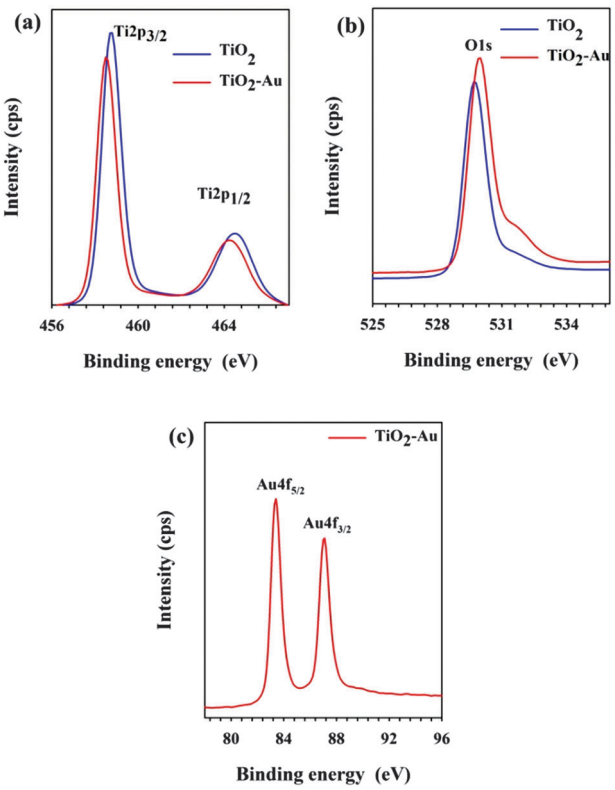

Fig. 2 XPS results for TiO_2–Au electrodes (a) Ti2p core spectra (b) O1s core spectra (c) Au4f core spectra.

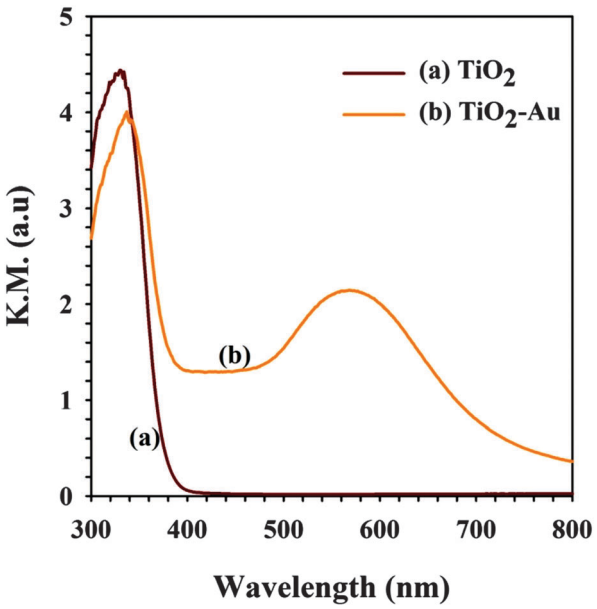

Fig. 3 Optical absorbance spectra (K.M. = Kulbelka–Munk) of TiO_2 and TiO_2–Au electrodes.

were recorded using standard three electrode systems. Fig. 4a shows the typical *J–V* plots of the TiO_2 NF electrode in dark and light. The observed current density under light illumination was nearly 50 times higher than the dark current, which could be attributed to the photogenerated charge carriers in pristine TiO_2. A similar response was observed for the TiO_2–Au HNF electrode under light illumination (Fig. 4b). The photohole assisted photoelectrocatalytic oxidation ability of pristine TiO_2 and TiO_2–Au HNFs was determined by adding 0.5 mM GSH in the electrolyte. As shown earlier in Scheme 1, it is anticipated that the successful PEC oxidation of GSH into GSSG might enhance the photocurrent. Thus, the enhancement of photocurrent in this system can be directly related to the PEC ability of TiO_2 and TiO_2–Au HNFs towards GSH bioanalysis.

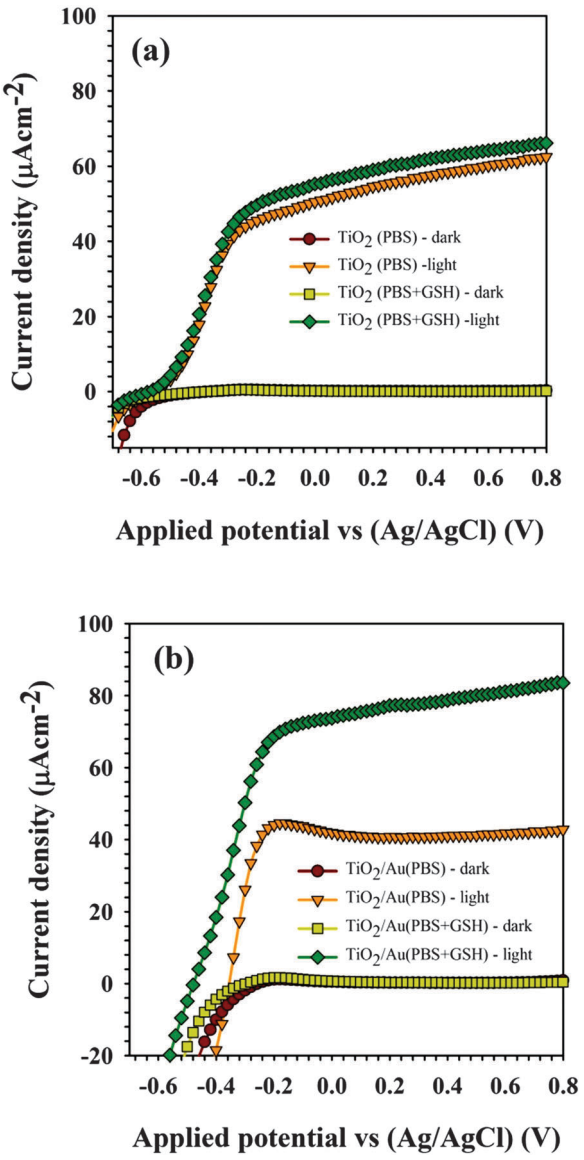

Fig. 4 *J–V* plots of (a) TiO_2 and (b) TiO_2–Au composite electrodes. The measurements were carried out using phosphate buffered saline (PBS) aqueous electrolyte. GSH (0.5 mM) is used in the electrolyte. Simulated solar light is used for illumination (100 mW cm^{-2}).

It is observed from Fig. 4a that addition of 0.5 mM GSH resulted in a negligible increase in photocurrent at the TiO_2 NF electrode, which can be attributed to the poor photogenerated charge carrier separation at the electrode/electrolyte interfaces and/or inadequate adsorption of GSH at the TiO_2/electrolyte interface.

In striking contrast, the addition of 0.5 mM GSH drastically improved the photocurrent generation by a factor of two (42.2 μA cm^{-2} to 84.4 μA cm^{-2}) at TiO_2–Au HNFs. This improvement may originate from Au NPs inclusion at the TiO_2 for several reasons: (a) increasing the visible light reception at TiO_2 through light scattering or the SPR effect, (b) promoting charge carrier separation at the TiO_2/Au interfaces, and (c) the high affinity of GSH molecules towards Au. Furthermore, it is observed that the onset potential of PEC GSH oxidation at TiO_2 NFs was observed at −0.35 V. The negative shift of the onset potential [−0.47 V *versus* silver/silver chloride (Ag/AgCl)] observed at TiO_2–Au HNFs implies that Fermi level pinning at the TiO_2/Au interfaces favors the photogenerated charge carrier separation. This negative potential of PEC GSH oxidation at TiO_2–Au HNFs electrode compared to the TiO_2 NF electrode is beneficial for the elimination of interference from other coexisting reductive species in the real time sample. Further increasing the applied potential higher than −0.25 V Ag/AgCl at the TiO_2 and TiO_2–Au electrode shows no change in the photocurrent generation, implying the saturation of GSH oxidation at this potential.

In order to ensure the possibility of contributing additional electrons from Au NPs to TiO_2 through the plasmonic effect (550 nm) for GSH oxidation, the PEC studies were performed using a ultraviolet (UV) cut-off filter (400 nm) (*J–V* plots not presented). It is well known that the UV cut-off filter will block the visible light at 400 nm and thus restrict the TiO_2 from the photoexcitation process, allowing the possibility of estimating the contribution of Au NPs in the PEC process. The TiO_2–Au HNFs showed very negligible photocurrent generation after blocking the visible light at 400 nm (Fig. S4, ESI†). This clearly shows that no plasmonic effect was observed in this system.

It is also significant in discussing the interaction between the anode material and GSH biomolecules that this could provide new insights into both selectivity and sensitivity. The biomolecule adsorption onto the electrode can be qualitatively determined by dark current measurements at TiO_2 and TiO_2–Au electrodes in the presence and absence of GSH biomolecules. Fig. S5 (ESI†) shows the *J–V* plots measured at dark conditions. The high dark current observed at the TiO_2–Au electrode compared to the pristine TiO_2 electrode is attributed to the Schottky junction formation. Further inclusion of GSH molecules in PBS electrolyte was found to lower the dark current. This implies that the GSH molecules adsorption on the electrode serves as a passivation layer to impede the electron from reacting with electrolyte directly. Such GSH adsorption onto the electrode may lead to high PEC oxidation, and thus produces a significant difference in PEC current generation in Fig. 4b. This effective interaction between GSH and the Au surface may be attributed to the formation of Au–x (x = N, O and S), by attracting thiol groups or intramolecular backbone hydrogen bonding of GSH.[56] The predominant

interaction mechanism between GSH and Au was verified by using a GSH derivative that lacks hydrogen bonding, GSSG. Fig. S6a (ESI†) shows the chronoamperometric response of the TiO_2–Au electrode in the presence of equal amounts of GSH and GSSG. It is found that the photocurrent generated for GSH at the TiO_2–Au electrode is twice that of GSSG. This clearly indicates that there is intramolecular backbone hydrogen bonding of GSH with Au and thus the "hydrogen bonding" mechanism is dominating in this system.

On the basis of these observations, the photoelectrocatalytic biosensing ability of TiO_2 and TiO_2–Au HNF electrodes using chronoamperometric measurements has been explored further. Fig. 5a shows the chronoamperometric response of the TiO_2 electrode obtained by successive addition of GSH under −0.33 V *versus* Ag/AgCl applied potential. Upon visible light irradiation, the photocurrent density at the TiO_2 NF electrode increases from 0 to 28 μA cm^{-2}. Furthermore, this TiO_2 NFs electrode responded quickly to the successive addition of GSH with a steady photocurrent increase up to 1.5 mM. The photocurrent reaches the saturation level at 2 mM GSH after which any further increase in GSH concentration does not produce any change in the photocurrent production (Fig. 5b). The limit of detection (LOD), defined as $I_{BLANK} + 3s_{BLANK}$, for the pristine TiO_2 NF was estimated to be 17 μM with a broad detection range between 0 to 2.0 mM. A wide linear detection range between 0.025 to 1.5 mM was obtained for GSH detection. The detection range of pristine TiO_2 NFs (our work) is comparable with porphyrin modified TiO_2.[33] On the other hand, TiO_2–Au HNFs show high dark current ~−40 μA cm^{-2} compared to pristine TiO_2 HNF at a similar applied potential (−0.33 V *versus* Ag/AgCl) (Fig. 5c). This might be attributed to the electron passage from TiO_2 to the electrolyte through the Au NPs Schottky junction as discussed previously (Fig. S4, ESI†). This dark current value was found to be decreased by increasing the GSH concentration in the electrolyte. This implies that the GSH molecules are adsorbed onto the Au NP surfaces and thus they impede the electron passage from Au NPs to the electrolyte. Fig. 5d shows the calibration plot of photocurrent density *versus* GSH concentration at the TiO_2–Au HNFs electrode. The photocurrent density was found to increase steadily with the successive addition of GSH. A linear detection range between 0.022 to 0.7 mM of GSH is observed with LOD of 0.002 mM GSH using the TiO_2–Au electrode.

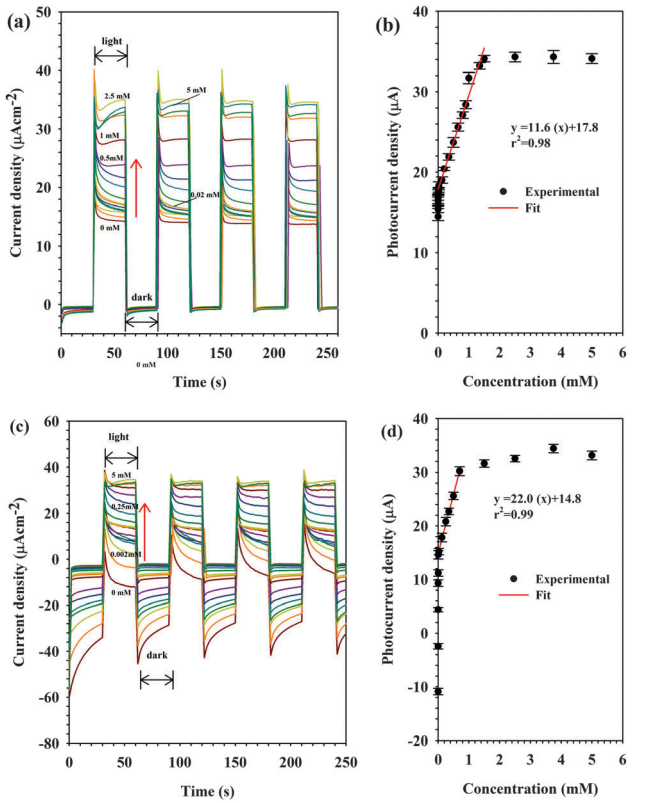

Fig. 5 Chronoamperometry plots of PEC GSH bioanalysis using (a) TiO_2 and (c) TiO_2–Au photoanodes; linear fit relationship between photocurrent generation and GSH concentration at different photoelectrodes (b) TiO_2 and (d) TiO_2–Au photoanodes. The measurements were carried out at −0.33 V *versus* Ag/AgCl using PBS aqueous electrolyte. Simulated solar light is used for illumination (100 mW cm^{-2}).

It was observed that both TiO_2 and TiO_2–Au HNF electrodes show a comparable linear detection range in this system. It is worth mentioning that the response range observed in this system was wider than that given in earlier reports using electrogenerated chemiluminescence of QDs (0.024–0.214 mM),[22] the fluorometric method (0.025–0.25 mM),[57] and surface-enhanced Raman scattering (0.1–0.8 μM). The LOD observed in this work (0.002 mM) is lower than that obtained with the previous methods, and it is worth mentioning that the improved upper LOD (>5 mM) shows that the photoelectrochemical detection of GSH is more suitable for use in biological samples, because the normal level of GSH in human fluids is in the range of 0.1–10 mM.[33,58] The selectivity of PEC detection of GSH using TiO_2 NFs and the TiO_2–Au HNF electrode was confirmed by measuring the response in the presence of interfering molecules. Fig. 6 shows the chronoamperogram of TiO_2 NFs and TiO_2–Au HNFs recorded with the interference of ascorbic acid and glucose.

It was found that the photocurrent response of TiO_2 NFs was affected by the presence of ascorbic acid and glucose. Strikingly, the TiO_2–Au HNF electrodes show a very negligible change in the photocurrent response with the addition of ascorbic acid and glucose, resulting in a very distinct dominant response exclusively to GSH oxidation. Although pristine TiO_2 electrodes show GSH linear detection with a wide range which is comparable with detection obtained with the TiO_2–Au electrode, it is inferior in GSH selectivity in the presence of other biological species. The high specificity of TiO_2–Au HNFs towards PEC GSH oxidation makes it a potential candidate for real time PEC GSH analysis. Furthermore, the electrospun derived fibrous coating can be directly implemented as ready-to-use "dip and read" type biosensors[59] or applied bias driven electrochemical biosensors.[60] However, it is worth mentioning that the interference analysis with cysteine shows noticeable interference during the detection of GSH at the TiO_2–Au electrode (Fig. S6b, ESI†). This is possibly because of the similar

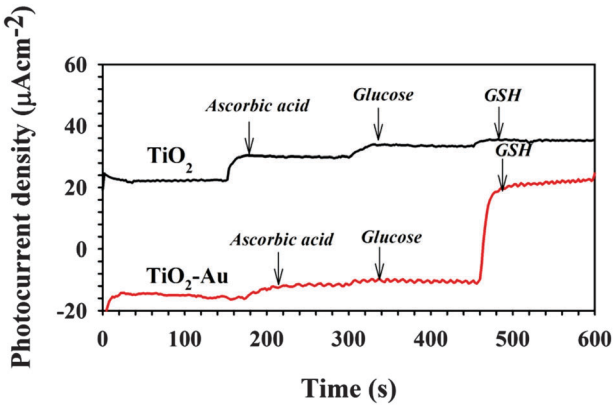

Fig. 6 Chronoamperometry plots showing the selectivity of TiO_2 (black line) and TiO_2–Au HNFs (red line). The measurements were carried out using a PBS aqueous electrolyte. Simulated solar light is used for illumination (100 mW cm^{-2}).

oxidation potential of cysteine and GSH. This can be addressed by introducing the intermediate molecules such as catechol which undergoes an electrochemical oxidation to form an *o*-quinone that can mediate in the reaction with a thiol, RSH, to form RSSR to eliminate the interference.[61,62] A detailed examination is needed to address this issue and is in progress.

Conclusions

The electrospun TiO_2–Au HNFs display enhanced photoelectrocatalytic activity towards GSH bioanalysis when compared to the pristine TiO_2 NFs under identical conditions. The electrochemical analysis on the nano–bio interface implies that the presence of Au NPs improves the adsorption of GSH molecules onto the electrode surface because of their higher affinity towards thiol molecules. Thus, the process of GSH adsorption onto the TiO_2–Au surface readily promotes the PEC oxidation of GSH, and thus results in a wide GSH detection range with high specificity towards the presence of interference molecules such as ascorbic acid and glucose. As a result, TiO_2–Au HNFs showed a linear detection range from 22 μM to 0.7 mM with high selectivity of GSH compared to the pristine TiO_2 electrode. The experimental results suggested that the single-step TiO_2–Au HNF fabrication technique reduces the material consumption more than the multi-step metal–metal oxide composite preparation techniques, and thus is anticipated to be attractive for a wide range of electrochemical and photoelectrochemical devices. The shape controlled TiO_2–Au HNF without fiber aggregation could be useful in the future in biosensing applications for the detection of a wide range of molecules. The analysis of charge transfer kinetics at the electrode/electrolyte interfaces is significant for extending the selectivity and sensitivity of the electrodes.

Experimental

Electrospun TiO_2–Au composite NF fabrication

The TiO_2 and TiO_2–Au HNFs were prepared using an electrospinning technique as follows. Typically, titanium tetraisopropoxide [$Ti(OiPr)_4$, Aldrich, 3 g] was mixed with acetic acid (2 mL) and ethanol (2 mL) and stirred for 10 minutes. The solution obtained was added to ethanol (3 mL) that contains PVP (Aldrich, $M_w \approx$ 1 300 000, Aldrich, 0.3 g) and the mixture is stirred uniformly for 20 min. For TiO_2–Au composite NFs, a known amount of tetrachloroaurate trihydrate ($HAuCl_4 \cdot 3H_2O$, Sigma-Aldrich, 0.03 g) was added to the titania precursor solution and mixed completely using a magnetic stirrer for 20 min. The resultant mixture is loaded into electrospinning syringe. The solution feeding rate to the nozzle is controlled with an automatic microcontroller at the rate of 1.0 mL h^{-1}. The applied voltage of 12 kV is applied to the nozzle. The distance between the collector and nozzle is maintained at 12 cm for generating the nanofibers. The electrospinning process is conducted at ambient conditions. After this process, the fibrous samples are subsequently treated with ethanol to improve their physical contact with the substrate. Finally, TiO_2 and TiO_2–Au NFs are sintered at 500 °C for 1 h under atmosphere of air.

Characterization

The surface morphology of TiO_2 and TiO_2–Au NFs was characterized using a field emission scanning electron microscope (FE-SEM, JSM-7600F, JEOL, Tokyo, Japan) and a field emission high-resolution transmission electron microscope (HR-TEM, JEM-2100F, JEOL, Tokyo, Japan). The chemical environment of pristine TiO_2 and TiO_2–Au NFs was analyzed using XPS with an angular resolved electron analyzer with a monochromated Al Kα source (AXIS Nova, Kratos Analytical). The optical diffuse reflectance spectra of the electrodes were recorded in the range of 350–900 nm using a V-670 JASCO UV-Vis spectrophotometer. The absorbance of the electrodes was estimated directly using the Kulbelka–Munk relationship with in-built software from the JASCO UV-Vis spectrometer.

Photoelectrochemical measurements

The PEC analysis was done using a three electrode configuration. The as-prepared TiO_2 and TiO_2–Au NF electrodes (electrode area: 1 cm^2) were used as the working electrode, Ag/AgCl as the reference and Pt foil as the counter electrode. PBS (0.1 M; Sigma-Aldrich, pH = 7.1) was used as the electrolyte for all PEC measurements. Cyclic voltammograms were recorded using the advanced potentiostat (PGSTAT-30, Metrohm Autolab) with the scanning rate of 50 mV s^{-1}. The photocurrent measurements were recorded using a solar simulator with a 300 W xenon arc lamp (HAL 320 W, Asahi Spectra). The light intensity (100 mW cm^{-2}) was calibrated using a silicon photodiode. The chronoamperometry analysis was carried out for TiO_2 and TiO_2–Au NFs and was tested with different GSH concentrations.

Acknowledgements

One of the authors, P. S., appreciates JSPS for providing a post-doctoral fellowship (ID: 13374).

References

1 A. Fujishima and K. Honda, *Nature*, 1972, **238**, 37–38.
2 P. Rodenas, T. Song, P. Sudhagar, G. Marzari, H. Han, L. Badia-Bou, S. Gimenez, F. Fabregat-Santiago, I. Mora-Sero, J. Bisquert, U. Paik and Y. S. Kang, *Adv. Energy Mater.*, 2013, **3**, 176–182.
3 P. Sudhagar, K. Asokan, E. Ito and Y. S. Kang, *Nanoscale*, 2012, **4**, 2416–2422.
4 P. Sudhagar, A. Devadoss, T. Song, P. Lakshmipathiraj, H. Han, V. V. Lysak, C. Terashima, K. Nakata, A. Fujishima, U. Paik and Y. S. Kang, *Phys. Chem. Chem. Phys.*, 2014, **16**, 17748–17755.
5 W.-W. Zhao, J.-J. Xu and H.-Y. Chen, *Chem. Soc. Rev.*, 2015, **44**, 729–741.
6 A. Devadoss, P. Sudhagar, S. Das, S. Y. Lee, C. Terashima, K. Nakata, A. Fujishima, W. Choi, Y. S. Kang and U. Paik, *ACS Appl. Mater. Interfaces*, 2014, **6**, 4864–4871.
7 Z. Yue, F. Lisdat, W. J. Parak, S. G. Hickey, L. Tu, N. Sabir, D. Dorfs and N. C. Bigall, *ACS Appl. Mater. Interfaces*, 2013, **5**, 2800–2814.
8 E. Golub, A. Niazov, R. Freeman, M. Zatsepin and I. Willner, *J. Phys. Chem. C*, 2012, **116**, 13827–13834.
9 W.-W. Zhao, J.-J. Xu and H.-Y. Chen, *Chem. Rev.*, 2014, **114**, 7421–7441.
10 M. Salari, S. H. Aboutalebi, A. Aghassi, P. Wagner, A. J. Mozer and G. G. Wallace, *Phys. Chem. Chem. Phys.*, 2015, **17**, 5642–5649.
11 S. Y. Chae, P. Sudhagar, A. Fujishima, Y. J. Hwang and O.-S. Joo, *Phys. Chem. Chem. Phys.*, 2015, **17**, 7714–7719.
12 J. Tang, J. Li, P. Da, Y. Wang and G. Zheng, *Chem. – Eur. J.*, 2015, **21**, 11288–11299.
13 N. H. P. Cnubben, I. M. C. M. Rietjens, H. Wortelboer, J. van Zanden and P. J. van Bladeren, *Environ. Toxicol. Pharmacol.*, 2001, **10**, 141–152.
14 M. Gutscher, A.-L. Pauleau, L. Marty, T. Brach, G. H. Wabnitz, Y. Samstag, A. J. Meyer and T. P. Dick, *Nat. Methods*, 2008, **5**, 553–559.
15 R. Deng, X. Xie, M. Vendrell, Y.-T. Chang and X. Liu, *J. Am. Chem. Soc.*, 2011, **133**, 20168–20171.
16 H. Liu, H. Wang, S. Shenvi, T. M. Hagen and R.-M. Liu, *Ann. N. Y. Acad. Sci.*, 2004, **1019**, 346–349.
17 F. Pinnen, P. Sozio, I. Cacciatore, C. Cornacchia, A. Mollica, A. Iannitelli, E. DAurizio, A. Cataldi, S. Zara, C. Nasuti and A. Di Stefano, *Arch. Pharm.*, 2011, **344**, 139–148.
18 R. Anandan, B. Ganesan, T. Obulesu, S. Mathew, K. K. Asha, P. T. Lakshmanan and A. A. Zynudheen, *Cell Stress Chaperones*, 2013, **18**, 121–125.
19 N. D. Goncharova, A. V. Shmaliy, V. Y. Marenin and S. A. Smelkova, *Bull. Exp. Biol. Med.*, 2007, **144**, 730–733.
20 D. Y. Wong, Y. L. Hsiao, C. K. Poon, P. C. Kwan, S. Y. Chao, S. T. Chou and C. S. Yang, *Cancer Lett.*, 1994, **81**, 111–116.
21 C.-C. Yeh, M.-F. Hou, S.-H. Wu, S.-M. Tsai, S.-K. Lin, L. A. Hou, H. Ma and L.-Y. Tsai, *Cell Biochem. Funct.*, 2006, **24**, 555–559.
22 Y. Wang, J. Lu, L. Tang, H. Chang and J. Li, *Anal. Chem.*, 2009, **81**, 9710–9715.
23 J. C. Harfield, C. Batchelor-McAuley and R. G. Compton, *Analyst*, 2012, **137**, 2285–2296.
24 L.-Y. Niu, Y.-S. Guan, Y.-Z. Chen, L.-Z. Wu, C.-H. Tung and Q.-Z. Yang, *J. Am. Chem. Soc.*, 2012, **134**, 18928–18931.
25 X. Chen, Y. Zhou, X. Peng and J. Yoon, *Chem. Soc. Rev.*, 2010, **39**, 2120–2135.
26 M. H. Pournaghi-Azar and F. Ahour, *J. Electroanal. Chem.*, 2008, **622**, 22–28.
27 J. Tang, Y. Wang, J. Li, P. Da, J. Geng and G. Zheng, *J. Mater. Chem. A*, 2014, **2**, 6153–6157.
28 J. Bai and B. Zhou, *Chem. Rev.*, 2014, **114**, 10131–10176.
29 D. Chen, H. Zhang, X. Li and J. Li, *Anal. Chem.*, 2010, **82**, 2253–2261.
30 X. Zeng, J. Bao, M. Han, W. Tu and Z. Dai, *Biosens. Bioelectron.*, 2014, **54**, 331–338.
31 J. Tang, Y. Zhang, B. Kong, Y. Wang, P. Da, J. Li, A. A. Elzatahry, D. Zhao, X. Gong and G. Zheng, *Nano Lett.*, 2014, **14**, 2702–2708.
32 Q. Han, K. Wang, L. Xu, X. Yan, K. Zhang, X. Chen, Q. Wang, L. Zhang and R. Pei, *Analyst*, 2015, **140**, 4143–4147.
33 W. Tu, Y. Dong, J. Lei and H. Ju, *Anal. Chem.*, 2010, **82**, 8711–8716.
34 J. Tang, B. Kong, Y. Wang, M. Xu, Y. Wang, H. Wu and G. Zheng, *Nano Lett.*, 2013, **13**, 5350–5354.
35 Y. Nakato, K. Ueda, H. Yano and H. Tsubomura, *J. Phys. Chem.*, 1988, **92**, 2316–2324.
36 V. Subramanian, E. Wolf and P. V. Kamat, *J. Phys. Chem. B*, 2001, **105**, 11439–11446.
37 F. P. García de Arquer, A. Mihi, D. Kufer and G. Konstantatos, *ACS Nano*, 2013, **7**, 3581–3588.
38 S. Mubeen, G. Hernandez-Sosa, D. Moses, J. Lee and M. Moskovits, *Nano Lett.*, 2011, **11**, 5548–5552.
39 C. Clavero, *Nat. Photonics*, 2014, **8**, 95–103.
40 M. D. Brown, T. Suteewong, R. S. S. Kumar, V. D'Innocenzo, A. Petrozza, M. M. Lee, U. Wiesner and H. J. Snaith, *Nano Lett.*, 2011, **11**, 438–445.
41 G. Chen, J. Wang, C. Wu, C.-Z. Li, H. Jiang and X. Wang, *Langmuir*, 2012, **28**, 12393–12399.
42 J. B. Priebe, J. Radnik, A. J. J. Lennox, M.-M. Pohl, M. Karnahl, D. Hollmann, K. Grabow, U. Bentrup, H. Junge, M. Beller and A. Brückner, *ACS Catal.*, 2015, **5**, 2137–2148.
43 P. Sudhagar, T. Song, A. Devadoss, J. W. Lee, M. Haro, S. Gimenez, C. Terashima, V. V. Lysak, J. Bisquert, A. Fujishima and U. Paik, *Phys. Chem. Chem. Phys.*, 2015, **17**, 19371–19378.
44 H. Zhao, B. Lu, J. Xu, E. Xie, T. Wang and Z. Xu, *Nanoscale*, 2013, **5**, 2835–2839.
45 H.-g. Wang, Y.-H. Li, W.-Q. Liu, Y.-C. Wan, Y.-w. Li and Q. Duan, *RSC Adv.*, 2014, **4**, 23125–23130.
46 P. Sudhagar, V. Gonzalez-Pedro, I. Mora-Sero, F. Fabregat-Santiago, J. Bisquert and Y. S. Kang, *J. Mater. Chem.*, 2012, **22**, 14228–14235.
47 P. S. Kumar, S. A. S. Nizar, J. Sundaramurthy, P. Ragupathy, V. Thavasi, S. G. Mhaisalkar and S. Ramakrishna, *J. Mater. Chem.*, 2011, **21**, 9784–9790.

48 G. Zhang, Z. Zhao, H. Tan, H. Zhao, D. Qu, M. Zheng, W. Yu and Z. Sun, *RSC Adv.*, 2015, **5**, 21237–21241.
49 J. Huang, T. Kunitake and S.-y. Onoue, *Chem. Commun.*, 2004, 1008–1009, DOI: 10.1039/b401071j.
50 S. Wang, H. Qian, Y. Hu, W. Dai, Y. Zhong, J. Chen and X. Hu, *Dalton Trans.*, 2013, **42**, 1122–1128.
51 N. Kruse and S. Chenakin, *Appl. Catal., A*, 2011, **391**, 367–376.
52 A. Y. Klyushin, T. C. R. Rocha, M. Havecker, A. Knop-Gericke and R. Schlogl, *Phys. Chem. Chem. Phys.*, 2014, **16**, 7881–7886.
53 E. A. Willneff, S. Braun, D. Rosenthal, H. Bluhm, M. Hävecker, E. Kleimenov, A. Knop-Gericke, R. Schlögl and S. L. M. Schroeder, *J. Am. Chem. Soc.*, 2006, **128**, 12052–12053.
54 X.-Q. Gong, A. Selloni, O. Dulub, P. Jacobson and U. Diebold, *J. Am. Chem. Soc.*, 2008, **130**, 370–381.
55 Z. Jiang, W. Zhang, L. Jin, X. Yang, F. Xu, J. Zhu and W. Huang, *J. Phys. Chem. C*, 2007, **111**, 12434–12439.
56 Z. Aliakbar Tehrani, Z. Jamshidi, M. Jebeli Javan and A. Fattahi, *J. Phys. Chem. A*, 2012, **116**, 4338–4347.
57 Z. Yao, X. Feng, C. Li and G. Shi, *Chem. Commun.*, 2009, 5886–5888, DOI: 10.1039/b912811e.
58 D. P. Jones, J. L. Carlson, V. C. Mody Jr, J. Cai, M. J. Lynn and P. Sternberg Jr, *Free Radicals Biol. Med.*, 2000, **28**, 625–635.
59 X. Ji, Z. Su, P. Wang, G. Ma and S. Zhang, *Analyst*, 2014, **139**, 6467–6473.
60 K. Mondal, M. A. Ali, V. V. Agrawal, B. D. Malhotra and A. Sharma, *ACS Appl. Mater. Interfaces*, 2014, **6**, 2516–2527.
61 P. T. Lee, D. Lowinsohn and R. G. Compton, *Electroanalysis*, 2014, **26**, 1488–1496.
62 P. T. Lee, D. Lowinsohn and R. G. Compton, *Analyst*, 2014, **139**, 3755–3762.